Journal of Molecular Catalysis A: Chemical 427 (2017) 45–53

Contents lists available at ScienceDirect

Journal of Molecular Catalysis A: Chemical

journal homepage: www.elsevier.com/locate/molcata

Editor's choice paper

$Ag/Bi_{12}O_{17}Cl_2$ composite: A case study of visible-light-driven plasmonic photocatalyst

Fei Chang[a,*], Xiaofang Wang[a], Jieru Luo[a], Jie Wang[a], Yunchao Xie[a], Baoqing Deng[a], Xuefeng Hu[b,*]

[a] School of Environment and Architecture, University of Shanghai for Science and Technology, Shanghai 200093, PR China
[b] Key Laboratory of Coastal Environmental Processes and Ecological Remediation, Yantai Institute of Coastal Zone Research, Chinese Academy of Sciences, Yantai, Shandong 264003, PR China

ARTICLE INFO

Article history:
Received 13 August 2016
Received in revised form
19 November 2016
Accepted 21 November 2016
Available online 21 November 2016

Keywords:
$Bi_{12}O_{17}Cl_2$
Ag
Plasmonic
Photocatalysis
Photocatalytic mechanism

ABSTRACT

In this investigation, novel $Ag/Bi_{12}O_{17}Cl_2$ plasmonic composites with different Ag contents were constructed through a solvothermal and subsequent photoreduction route and fully characterized by a collection of analytical techniques. Spectroscopic results confirmed the presence and uniform dispersion of Ag nanoparticles on the 2D nanosheets of $Bi_{12}O_{17}Cl_2$. The Ag content in composites exerted considerable influence on the extension of light-adsorption range and the enlargement of specific surface areas. The photocatalytic abilities of these $Ag/Bi_{12}O_{17}Cl_2$ composites were evaluated toward the degradation of rhodamine B (RhB) and 2,4-dichlorophenol (2,4-DCP) under the visible-light irradiation. The results demonstrated that the $Ag/Bi_{12}O_{17}Cl_2$ composites showed much higher photocatalytic efficiencies than that of pure $Bi_{12}O_{17}Cl_2$, especially the sample with an optimal Ag content showing the best photocatalytic behavior among all tested samples. The remarkable enhancement of $Ag/Bi_{12}O_{17}Cl_2$ photocatalytic efficiency could be mainly attributed to the efficient charge separation that was induced by the localized surface plasmon resonance effect of metallic Ag, strong visible-light adsorption and the favorable morphology with enlarged specific surface areas. Eventually, the photocatalysis mechanism over $Ag/Bi_{12}O_{17}Cl_2$ composites was preliminarily proposed on the base of reactive species trapping experiments.

1. Introduction

Over the past several decades, heterogeneous photocatalytic processes have drawn ever growing interest since they are able to find potential applications in energy storage and environmental remediation by means of absorbing and converting solar to chemical energy [1–3]. Bismuth oxychloride, a group of V-VI-VII ternary semiconductors, featured with a lamellar structure composed of [Cl-Bi-O-Bi-Cl] slices packed together with van der Waals force through chlorine atoms along the *c*-axis [4]. The laminated structure induces the generation of internal electric field that promotes the separation of photoproduced electron-hole pairs, thus favoring the improvement of photocatalytic performance [5]. However, the bare BiOCl is merely sensitive to UV light due to the large band gap and thus exhibits poor photocatalytic capability in visible-light region [6]. Under specific conditions, the wide band gap can be tuned by simply changing the chemical composition of BiOCl to form chlorine-deficient and oxygen-rich analogues, such as $Bi_{12}O_{17}C_{l2}$, a typical bismuth oxychloride candidate with suitable band structures, thus attracting enormous attention in terms of photocatalytic degradation and selective oxidation under the visible-light illumination [7–9].

The photocatalytic efficiency of bare $Bi_{12}O_{17}C_{l2}$ can be improved by the morphological tailoring or the integration with other appropriate components [10–12]. Adequate morphologies such as nanowires, nanobelts, nanoplates, and three-dimensional hierarchical microflowers achieved by various synthetic protocols, are beneficial to shorten diffusion pathways, strengthen interfacial charge separation, and enhance light harvesting, therefore promoting photocatalytic degradation ability. The latter is relevant to the generation of heterojunction structures by coupling several semiconductor componenets with appropriate electronic structures, which endows the obtained composites with the prolonged lifetime of carries and extended adsorption in visible-light region [13,14]. He et al. prepared $Bi_{12}O_{17}C_{l2}/\beta$-$Bi_2O_3$ composites that exhibited excellent catalytic performance towards degradation of

* Corresponding authors.
E-mail addresses: feichang@usst.edu.cn (F. Chang), xfhu@yic.ac.cn (X. Hu).

http://dx.doi.org/10.1016/j.molcata.2016.11.028
1381-1169/

4-*tert*-butylphenol upon visible-light illumination [11]. A heterojunction composite BiOI/$Bi_{12}O_{17}C_{l2}$ was synthesized by Bi et al. and displayed outstanding photocatalytic behavior over methyl orange and phenol under visible light [13]. Quite recently, the $Bi_{12}O_{17}C_{l2}/MoS_2$ Janus bilayer junctions could efficiently steer the charge flow by the internal electric field and thus showed superior visible-light hydrogen evolution ability [14].

Besides, another strategy to attain excellent visible-light photocatalytic performance is to incorporate plasmonic metal nanoparticles onto the semiconductors surface [15–17]. These plasmonic metal nanoparticles, like Ag a low cost and toxicity metal, induce the localized surface plasmonic resonance (LSPR) effect that boosts photocatalytic processes through the extension of light adsorption scope, increase of incident light scattering, and efficient transfer of plasmonic energy from metal nanoparticles to semiconductors to produce more charge carries. Besides, these metal nanoparticles can role as sinks to trap electrons flowed from semiconductors upon excitation, which facilitates the separation of photogenerated electron-hole pairs. Till now, several cases of Ag/bismuth oxyhalide plasmonic photocatalysts have been reported [18–20]. However, to the best of our knowledge, the synthesis and photocatalytic evaluation of Ag/$Bi_{12}O_{17}Cl_2$ composites have never been investigated.

Herein, in this study, a facile photoreduction method was adopted to fabricate Ag/$Bi_{12}O_{17}Cl_2$ plasmonic composites that were systematically characterized by a collection of analytical techniques. The existence of crystalline metallic Ag nanoparticles was recognized by the XPS, SEM, EDS, and UV–vis DRS spectra. With the raise of Ag content, the extension of light absorption range and the enhancement of visible-light harvesting were achieved. These Ag/$Bi_{12}O_{17}Cl_2$ plasmonic composites showed much higher photocatalytic degradation efficiency over both organics RhB and 2,4-DCP than bare $Bi_{12}O_{17}Cl_2$, primarily ascribing to the synergistic effect of the favorable textural, optical, and electronic properties. Finally, a possible photocatalysis mechanism was proposed according to the active species trapping experiments.

2. Experimental

2.1. Chemicals

Bismuth (III) nitrate pentahydrate ($Bi(NO_3)_3{\cdot}5H_2O$, AR), hydrochloric acid (HCl, 36 ~ 38%, AR), sodium hydroxide (NaOH, AR), silver nitrate ($AgNO_3$, AR), isopropanol alcohol (IPA, AR), disodium ethylenediaminetetraacetate dihydrate (EDTA-2Na, AR), nitroblue tetrazolium (NBT, AR), 2,4-dichlorophenol (2,4-DCP, AR) and other chemical reagents involved were supplied by Sinopharm Chemical Reagent Co., Ltd. (Shanghai, China). Rhodamine B (RhB, AR) was purchased from Shanghai SSS Reagent Co., Ltd. (Shanghai, China). All chemicals were used as received without further purification and deionized water was used throughout the experimental.

2.2. Materials preparation

2.2.1. Synthesis of sample $Bi_{12}O_{17}Cl_2$

The sample $Bi_{12}O_{17}Cl_2$ was synthesized in the light of a reference with a small modification [10]. Typically, $Bi(NO_3)_3{\cdot}5H_2O$ (3.84 mmol) was dissolved into a HCl aqueous solution (2 M, 25 mL) and the resultant transparent mixture was dropped with a NaOH aqueous solution (4 M, 20 mL). The obtained suspension was allowed to vigorously stir for 0.5 h at room temperature and subsequently transferred into a 100 mL stainless-steel Teflon-lined autoclave. After staying at 160 °C for 6 h and then cooling to room temperature, the yellow precipitate was finally collected, washed with deionized water and absolute ethanol for several times, and dried at 60 °C overnight to give $Bi_{12}O_{17}Cl_2$ as a yellow powder.

2.2.2. Synthesis of Ag/$Bi_{12}O_{17}Cl_2$ plasmonic composites

An aqueous suspension (40 mL) containing as-prepared sample $Bi_{12}O_{17}Cl_2$ (1 g) was sonicated for 0.5 h and then was added with a desired amount of $AgNO_3$. After continuously stirred for 4.5 h at room temperature and dropwise added with methanol (20 mL) in dark, the resultant mixture was subjected to an exposure to a 400 W halogen lamp (Institute for Electric Light Source, Beijing) equipped with a $NaNO_2$ solution (2 M) to remove ultraviolet light (<400 nm). After 20 min irradiation, the photo-reduction reaction was stopped and the precipitate was collected by centrifugation, rinsed with deionized water and absolute ethanol for several times, and dried at 60 °C for 12 h to give a target composite Ag/$Bi_{12}O_{17}Cl_2$. For convenience, the as-prepared Ag/$Bi_{12}O_{17}Cl_2$ series were nominated as ABx and x hereafter referred to a theoretical mass percentage of Ag verse $Bi_{12}O_{17}Cl_2$. N-doped TiO_2 (N-TiO_2) was also constructed according to a previous report for comparison [21].

The exact Ag content was measured by an ICP-OES apparatus using a procedure described as follows: 0.1 g ABx sample was added into a Teflon digestion tank and a concentrated nitric acid (65%-68%, 15 mL) was subsequently added. The mixture was heated and digested at 200 °C until a suspension around 0.5 mL was obtained. Afterwards, a concentrated nitric acid (65%-68%, 5 mL) was added and the resultant mixture was undergone a same digestion protocol to ensure the complete dissolution. The remained clear solution (0.5 mL) was diluted with the nitic acid solution (7.6%) to 500 mL and then was analyzed. The Ag content in sample AB2, AB4, AB6, and AB8 was 0.70%, 0.90%, 1.26%, and 0.80%, respectively. Since the content of samples quite differentiated to the theoretical amount, the Ag content remained in mother liquid was further checked by using ICP-OES and was 1.10%, 2.82%, 4.80%, and 6.71%. The total Ag content by the integration of target sample and mother liquid was approximately in accordance with the initial addition amount. We speculated that with the increase of Ag initial concentration, the generated Ag nanoparticles tended to agglomerate to a separate phase from the surface of $Bi_{12}O_{17}Cl_2$ substrate and were thus easily removed along with the mother liquid, which were supported by the mother liquid as a grey suspension and ICP-OES results.

2.3. Characterization

The crystalline structures and compositions of samples were measured by powder X-ray diffraction (XRD) patterns on a Bruker D8 Advance X-ray diffractometer (Bruker AXS, Germany) using a Cu Kα radiation source (λ = 1.5406 Å). The valence-band X-ray photoelectron spectroscopy (VB XPS) spectrum and X-ray photoelectron spectroscopy (XPS) measurements were conducted on a Thermo Scientific ESCALAB 250×i system. Binding energies were calibrated with the adventitious carbon (C1s = 284.6 eV). The morphology and microstructure of obtained samples were recorded by a transmission electron microscope (TEM, JEOL JEM-2011) and a scanning electron microscope (SEM, Hitachi S-4700) equipped with an X-ray energy dispersion spectroscope (EDS). The specific surface areas were evaluated by nitrogen adsorption-desorption isotherms at 77 K by using a Micromeritics 3Flex apparatus. Before measurements, all samples were degassed at 423 K under vacuum over 6 h. UV–vis diffuse reflectance spectra (UV–vis DRS) were obtained on a Shimadzu UV-2600 spectrophotometer using $BaSO_4$ as a reference. Photoluminescence (PL) spectra were recorded on a Shimadzu RF-5301 PC Fluorescence spectrophotometer with an excitation wavelength of 324 nm. The Ag content was evaluated by an ICP-OES apparatus (PerkinElmer Optima 8000)

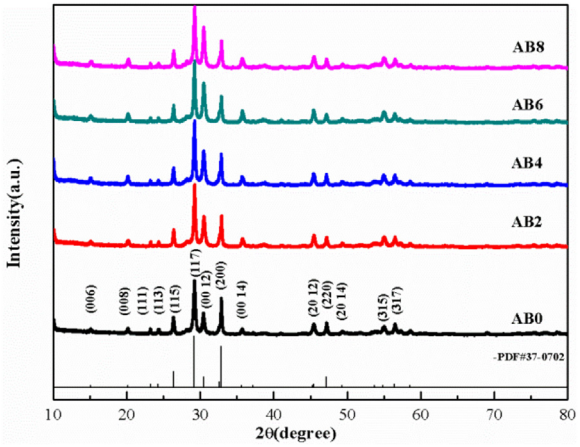

Fig. 1. XRD patterns of Ag/$Bi_{12}O_{17}Cl_2$ series.

2.4. Photocatalytic activity measurement

Photocatalytic evaluations were performed toward the degradation of dye RhB and 2,4-DCP under visible-light irradiation using a 300 W xenon lamp (CEL-HXF300, AuLight, Beijing) equipping with a 420–780 nm cut-off filter. 40 mg of the photocatalyst was added to and dispersed in 80 mL RhB (15 mg L^{-1}) or 2,4-DCP (10 mg L^{-1}) aqueous solutions. The distance between the light source and the surface of reaction solution was fixed as 20 cm. Prior to irradiation, the suspension was vigorously stirred in dark for 1 h to reach an adsorption–desorption equilibrium between contaminant molecules and surface of photocatalysts. At the irradiation time intervals of every 30 min, a 3 mL aliquot was collected and then centrifuged (10000 rpm, 5 min) to remove catalyst nanoparticles. The residue concentration of RhB and 2,4-DCP was analyzed through a UV–vis spectrophotometer (Purkinje General T6) at 554 nm and a UV–vis spectrophotometer (Shimadzu UV-2600) at 281 nm, respectively.

To detect active radical species generated in photocatalytic process, 1.0 mM IPA and EDTA-2Na were introduced in the presence of composite AB4 during photocatalytic experiments for capturing hydroxyl radicals (•OH) and holes (h^+), respectively [22,23]. The formation of superoxide radicals (•O_2^-) was checked by adding 25 μM NBT in the place of RhB in solution [24]. The presence of •OH and •O_2^- radicals was further examined by 5,5-dimethyl-1-pyrroline-N-oxide (DMPO) capture under deionized water for DMPO-·OH and methanol for DMPO-·O_2^- by using the ESR technique on a FA200 spectrometer.

The reusability and durability of composite AB4 were evaluated under a same condition as above. Specifically, after each run, the photocatalyst was carefully collected from the reaction medium by centrifugation, rinsed by deionized water and ethanol for several times, and dried at 60 °C overnight for the next cycling experiment.

3. Results and discussion

XRD patterns of plasmonic composites Ag/$Bi_{12}O_{17}Cl_2$ and pure $Bi_{12}O_{17}Cl_2$ are displayed in Fig. 1. Clearly, all diffraction peaks of sample AB0 are well-resolved and can be unambiguously assigned to the pure tetragonal-phase $Bi_{12}O_{17}Cl_2$ (JCPDS No. 37-0702). After the decoration of Ag, those composites exhibit quite similar diffraction patterns to pure $Bi_{12}O_{17}Cl_2$, revealing that the existence of Ag species exerts insignificant influence on the crystallinity. Besides, the negligible variety of all peak positions and lattice parameters of $Bi_{12}O_{17}Cl_2$ in composites confirms that the Ag species deposit on the surface, instead of into the $Bi_{12}O_{17}Cl_2$ lattice. In addition, a slight change of peak intensity ratio (117)/(00 12) is clearly observed and can be attributed to the variation of preferred orientation induced by the sonication treatment during the photoreduction synthesis [25]. The absence of corresponding diffraction peaks of metallic Ag may possibly assigned to the low content and good dispersion of Ag species onto the surface of $Bi_{12}O_{17}Cl_2$. Besides, characteristic peaks assigning to impurities or other phases are undetectable, demonstrating the high purity of these as-prepared composites.

To verify the presence of metallic Ag and check surface valence states of AB composites, XPS analysis of the composite AB4 was carried out and shown in Fig. 2. The survey spectrum in Fig. 2A identifies the presence of several elements Bi, O, Ag, Cl and adventitious C, as expected. Fig. 2B displays the valence-band X-ray photoelectron spectroscopy (VBXPS) spectra, revealing that the position of valence-band maximum (E_{VB}) of composite AB4 is located at 2.02 eV that is quite close to the reported value [8]. Both prominent peaks with binding energies at about 159.31 eV and 164.64 eV in Fig. 2C are ascribed to Bi $4f_{7/2}$ and Bi $4f_{5/2}$ of chemical states of Bi^{3+} in lattice, which is in good accordance with the previous reports [20]. The high resolution spectrum of the Ag 3d in Fig. 2D displays two peaks with binding energies located at 373.63 eV and 367.63 eV, corresponding to Ag $3d_{3/2}$ and Ag $3d_{5/2}$, respectively. The presence of both abovementioned peaks and the separation of 6.0 eV between binding energies ensure the formation of zero-valence Ag instead of Ag cations in composite AB4 [19]. The banding energy of Ag 3d5/2 is much smaller than that of metallic Ag (368.2 eV) and quite close to those in composites Ag/ZnO (367.6 eV) [26], Ag/g-C_3N_4 (367.8 eV) [27], and Ag/AgCl/$NaTaO_3$ (367.4 eV) [28], mainly attributing to the special interaction between metallic Ag and semiconductor $Bi_{12}O_{17}Cl_2$. Lu et al. attributed the low binding energy of Ag 3d5/2 to the evident positive charge of Ag induced by the efficient migration of electrons from Ag to ZnO that was driven by the relatively small work function of Ag in comparison to that of ZnO [26]. Similarly, it is reasonable to speculate that the work function of Ag herein may be smaller than that of another component $Bi_{12}O_{17}Cl_2$, which should be researched in detail in the future.

An in-depth observation for these plasmonic composites was further performed by SEM and TEM images, as shown in Fig. 3. Fig. 3A and B depict the typical morphological and microstructural images of samples AB0 and AB4. Evidently, numerous irregular two-dimensional nanosheets with a thickness of approximately 80 nm in sample AB0 tend to randomly aggregate to large clusters with smooth surfaces exposed. After the decoration of metallic Ag species through a photoreduction process, some brilliant cubic dots in a size ranging from several nanometers to 250 nm appear on surface of large clusters in sample AB4 in Fig. 3B, as marked by yellow arrows. To identify the chemical composition of these brilliant dots, two microregions without and with a dot labeled respectively by green and red circles were typically selected for EDS analyses. As expected, the EDS spectrum in Fig. 3C shows three elements of Bi, O, Cl and the atomic ratio of Bi:Cl is extremely close to the theoretical ratio of 6:1, indicating the existence of pure $Bi_{12}O_{17}Cl_2$ phase. The atomic proportion of O exceeds the stoichiometric ratio, resulted by the adsorption of oxygen-contained species, such as H_2O molecules and OH^- moieties. However, another EDS spectrum in Fig. 3D confirms the presence of Ag species, revealing that these brilliant cubic dots are indeed the metallic Ag nanoparticles. In addition, SEM images from sample AB2 to AB8 were shown in Fig. S1. The TEM images of sample AB0 and AB4 were displayed in Fig. 3E and F. Anomalous nanosheets are also observed in both composites and an obvious black dot appeared on surface in sample AB4 is definitely ascribed to a metallic Ag nanoparticle.

The optical property of as-prepared samples was evaluated by UV–vis diffuse reflectance spectra (UV–vis DRS). As displayed in Fig. 4A, the photoresponse of the sample AB0 ranges from the UV-light to visible-light region and the adsorption edge approaches up to 530 nm. After the integration of metallic Ag nanoparticles, these

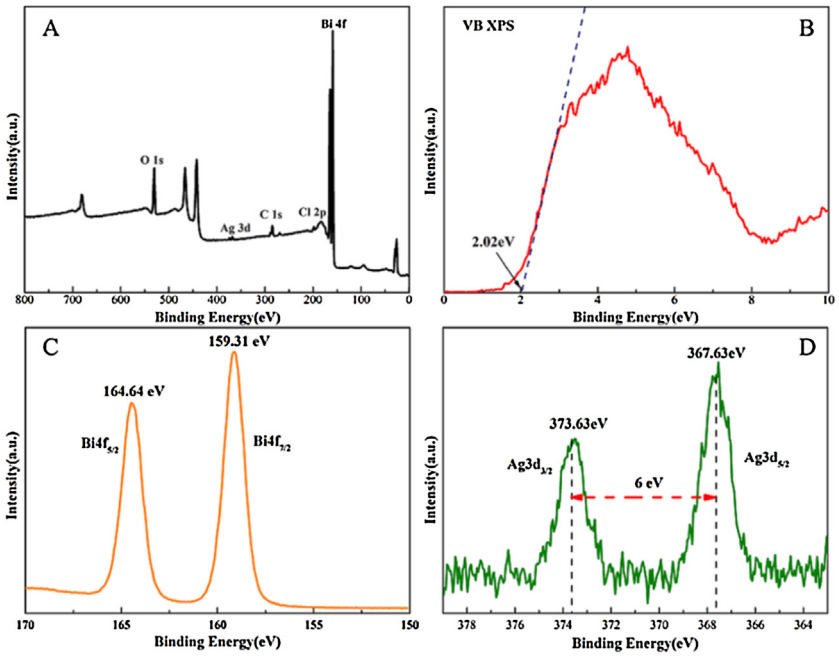

Fig. 2. XPS analysis of the composite AB4: (A) survey spectra, (B) VBXPS, (C) Bi 4f, and (D) Ag 3d.

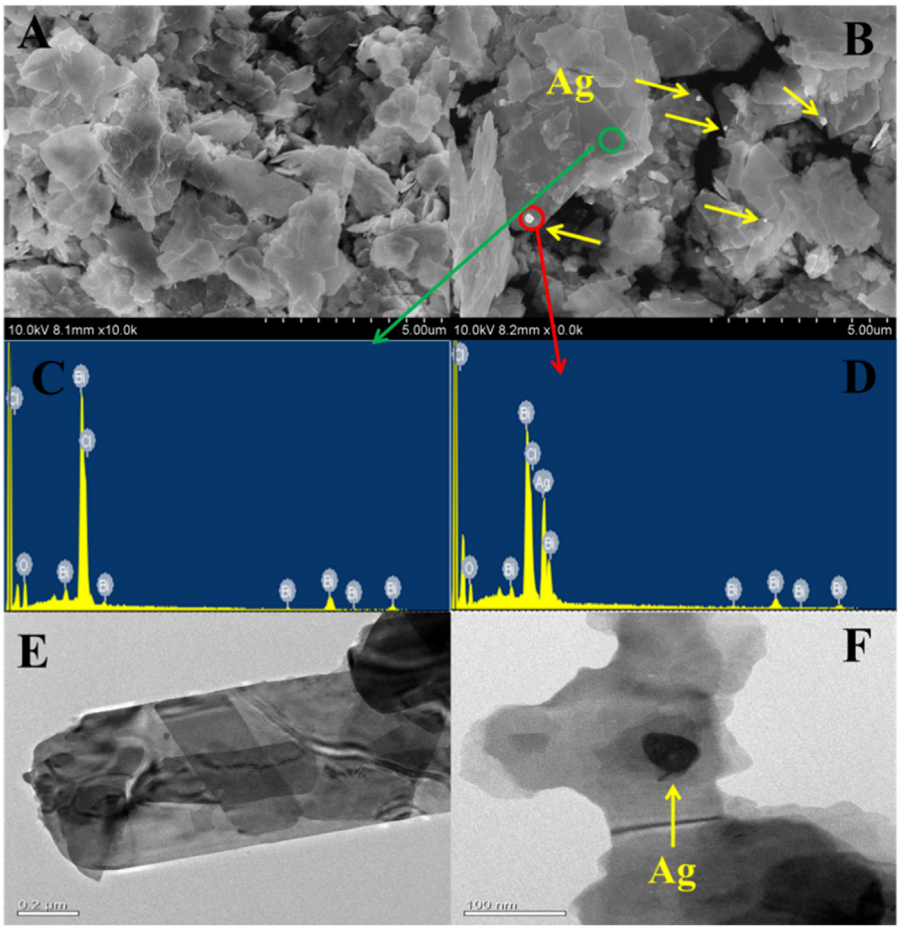

Fig. 3. SEM images of composites AB0 (A) and AB4(B), and the corresponding EDS spectra (C) and (D), TEM of the samplesAB0 (E) and AB4 (F).

composites show a similar absorption ability in UV-light region while an enhanced absorption in visible-light region in comparison to sample AB0, mainly attributing to the LSPR effect of plasmonic Ag species with the wide nanoparticles size distribution[29], as also represented in Fig. 3 and Fig. S1. Furthermore, the visible-light absorption of these composites strengthens with the increase of Ag

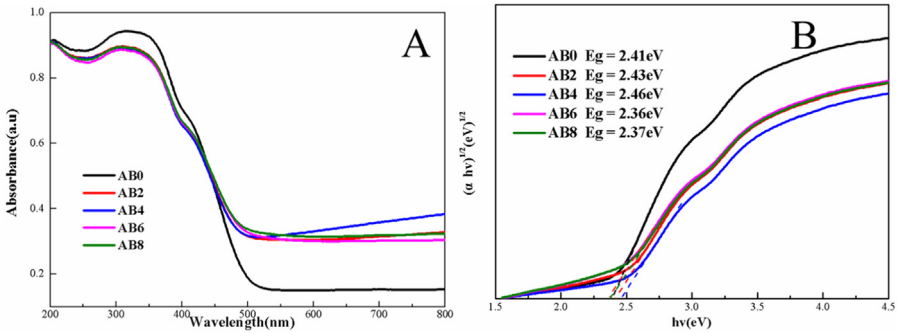

Fig. 4. (A) UV–vis diffuse reflectance spectra of $Ag/Bi_{12}O_{17}Cl_2$ series; (B) a plot of $(\alpha h\nu)^{1/2}$ *vs.* photon energy ($h\nu$) of corresponding samples.

Table 1
S_{BET} pore volume, band gap, and apparent reaction rate constants of various samples.

Samples	S_{BET}($m^2\ g^{-1}$)	Pore volume($10^{-2}cm^3\ g^{-1}$)	Band gap(eV)	Apparent reaction rate constants	
				For RhB($10^{-3}\ min^{-1}$)	For 2,4-DCP ($10^{-3}\ min^{-1}$)
AB0	6.4	3.3	2.41	1.93	4.29
AB2	7.1	3.3	2.43	5.72	–
AB4	7.6	4	2.46	10.3	7.46
AB6	5.2	2.4	2.36	6.76	–
AB8	5.8	2.3	2.37	7.63	–
N-TiO_2	–	–	–	1.25	3.21

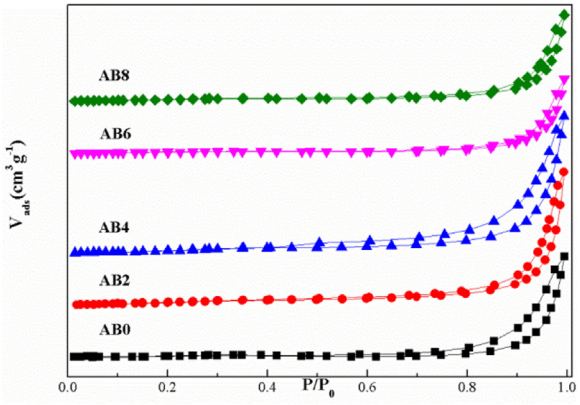

Fig. 5. Nitrogen adsorption–desorption isotherms of $Ag/Bi_{12}O_{17}Cl_2$ series.

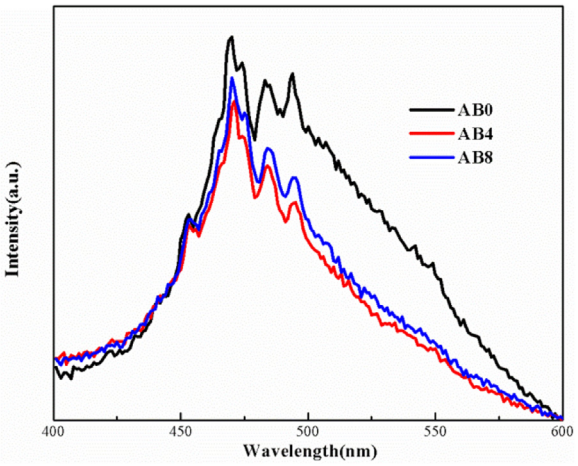

Fig. 6. The photoluminescence spectra of samples AB0, AB4, and AB8 at room temperature (λ_{Ex} = 324 nm).

content and then decrease when mass percentage of $Ag/Bi_{12}O_{17}Cl_2$ is beyond 4%, revealing that sample AB4 is of the strongest visible-light harvesting ability among all candidates and may potentially display excellent photocatalytic ability. The band gap energies of these samples were calculated following the formula:$\alpha h\nu = A(h\nu\text{-}E_g)^{n/2}$, where α, ν, E_g and A are the absorption coefficient, light frequency, band gap energy, and a constant, respectively. n is a constant that depends on the characteristic of transition in semiconductors, that is, direct transition ($n = 1$) or indirect transition ($n = 4$). The $Bi_{12}O_{17}Cl_2$ with the indirect transition was reported by previous literatures[7,8], and thus its band gap energy was estimated to be 2.41 eV in Fig. 4B. The variation trend of estimated band-gap energies is similar to that of visible-light absorption ability of these composites, as seen in Table 1.

The N_2 adsorption-desorption isotherms were measured to investigate the textural property of obtained samples. As represented in Fig. 5, the isotherms of AB series belong to the Type IV with a Type H3 hysteresis loop at a high relative pressure between 0.5 and 1.0, revealing the presence of slit-like pores that may possibly be formed from the inter-nanosheet stacking morphology [11]. The specific surface area values and pore volumes increased slightly and then decreased along with the increase of Ag precursor addition. The above phenomenon can be explained as follows. The introduction of appropriate amount of external Ag nanoparticles may cause the creation of new exposed surface and thus improve the specific surface area. However, the excess amount of Ag nanoparticles may inversely reduce the surface area by means of blocking stacking pores. As can be seen, the composite AB4 has the largest specific surface area among all samples, which is beneficial to adsorb organic contaminants around active sites and thus maximize the photocatalytic performance [30].

It is well realized that the photoluminescence (PL) spectroscopy is able to reflect the migration, transfer, and separation efficiency of photoinduced electron-hole pairs that directly affect the photocatalytic performance of semiconductors [31]. PL spectra of samples AB0, AB4, and AB8 were hereafter recorded and shown in Fig. 6. A broad intensive band with several weak peaks ranging from 400 to 600 nm is observed and ascribed to charge-transfer transitions between valance and conduction band, the surface-defect like oxygen vacancies generated from the fast growth rate, and different valence states of bismuth ions in $Bi_{12}O_{17}Cl_2$ [10,12]. The existence

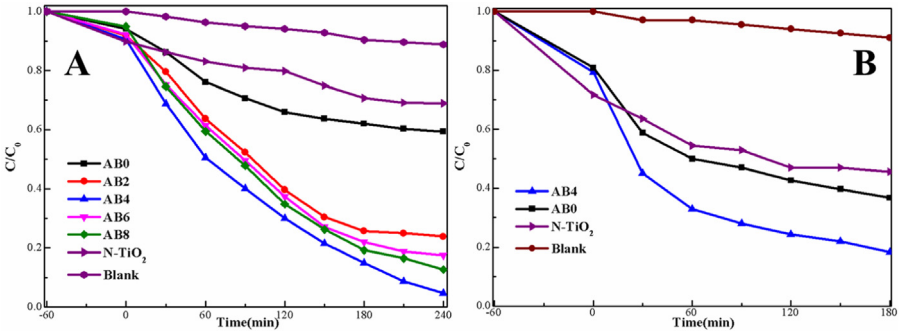

Fig. 7. Photocatalytic performances of various samples for the degradation of RhB (A) and 2,4-DCP (B) under visible-light irradiation.

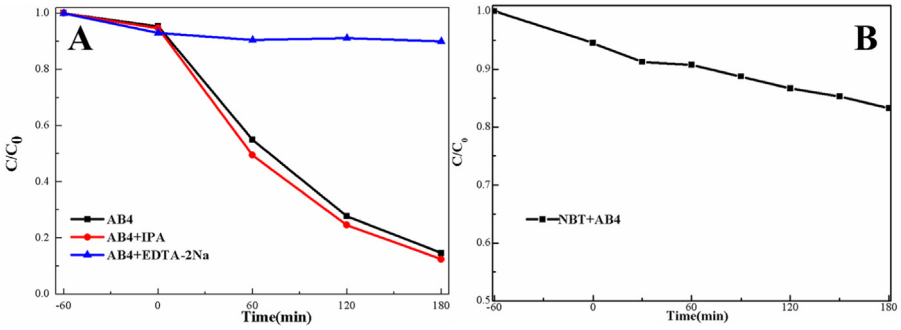

Fig. 8. Active species trapping experiments (A), and the transformation percentage of NBT concentration using the composite AB4 (B).

of deposited Ag can inhibit the radiative recombination of generated charge carriers [32]. Accordingly, the emission band intensity of the sample AB4 is weaker than those of samples AB0 and AB8, suggesting that the presence of appropriate amount of Ag is crucial to the efficient separation of photogenerated charge carries. Therefore, sample AB4 with the lowest band intensity is expected to show an excellent photocatalytic degradation efficiency basing upon UV–vis DRS and PL analyses.

From the aforementioned spectroscopic analyses, we can conclude that metallic silver nanoparticles were successfully formed via a photoinduced reduction process and uniformly dispersed on surface of $Bi_{12}O_{17}Cl_2$. In addition, composite AB4 possesses excellent visible-light harvesting ability and effective separation capability of charge carriers, potentially benefitting the enhancement of photocatalytic degradation of organic contaminants.

Photocatalytic degradation of RhB and 2,4-DCP over as-synthesized samples was evaluated under visible-light irradiation ($\lambda \geq 420$ nm), as shown in Fig. 7A. Dye RhB could not be significantly decomposed in absence of photocatalysts even after an irradiation time of 240 min, suggesting that the direct photolytic degradation can be ignored. Sample N-TiO_2 shows fairly low photocatalytic degradation efficiency around 30% after 240 min. Bare $Bi_{12}O_{17}Cl_2$ displays a moderate catalytic performance, by which around 40% RhB molecules were destroyed after 240 min. However, the deposition of metallic Ag on surface of $Bi_{12}O_{17}Cl_2$ ensures the significant enhancement of photocatalytic efficiency toward the degradation of RhB. In particular, with the raise of Ag content in plasmonic composites, the photocatalytic performance of as-obtained photocatalysts increases first and then declines when the content of metallic silver species exceeds 4%. As a result, under the identical condition sample AB4 is the best candidate among all samples and provide a maximal catalytic degradation efficiency of 93%. The apparent reaction rate constants were estimated through a pseudo-first-order kinetic equation that was simplified from the Langmuir-Hinshelwood kinetic model in diluted solutions [33], and are listed in Table 1. Correspondingly, the sample AB4 has the largest apparent reaction rate constant value that is almost 5.3 and 8.2 times as high as the samples AB0 and N-TiO_2, as also shown in Fig. S2.

To exclude the possibility of dye sensitization, 2,4-DCP as a colorless pollutant, was utilized to identify the visible-light-driven photocatalytic process, as depicted in Fig. 7B. Clearly, after an irradiation time of 180 min the composite AB4 exhibits a satisfactory photocatalytic efficiency about 82% that is much higher than those results from AB0 and N-TiO_2. The temporal evolution of the absorbance spectra of 2,4-DCP was recorded and shown in Fig. S3. Accordingly, the apparent reaction rate constant of the composite AB4 is 1.7 and 2.3 times as high as those from samples AB0 and N-TiO_2 in Fig. S2, respectively.

The enhancement of photocatalytic behavior of AB plasmonic series is mainly attributed to following aspects. Foremost, the integration of metallic Ag species strengthens the visible-light scattering and harvesting ability in visible-light region, favoring the generation of more electron-hole pairs for oxidative degradations. Second, the Ag nanoparticles are able to role as electron sinks to promote the efficient separation of produced charge carriers [34,35]. A suitable amount of Ag deposits facilitates the migration and transfer of excited electrons from the conduction band of semiconductor to metallic sites through the Schottky barrier generated at the metal-semiconductor interface. However, an excessive content of silver species acts as recombination centers for the photoinduced electron-hole pairs or cover active sites on surface to hinder the accessibility and incoming visible light, thus diminishing the photocatalytic degradation efficiency [18,19]. Thirdly, the LSPR effect of metallic Ag species excited by the absorption of visible light with specific frequency would promote the surface electron excitation and interfacial electron transfer, and thus be propitious to the enhanced photocatalytic efficiency [5,36]. Last but not the least, the suitable electronic property and morphology with enlarged specific surface areas may also contribute to the increased photocatalytic performance. The former ensures the moderate band gap energy that can be easily excited and trigger photocatalytic process and the

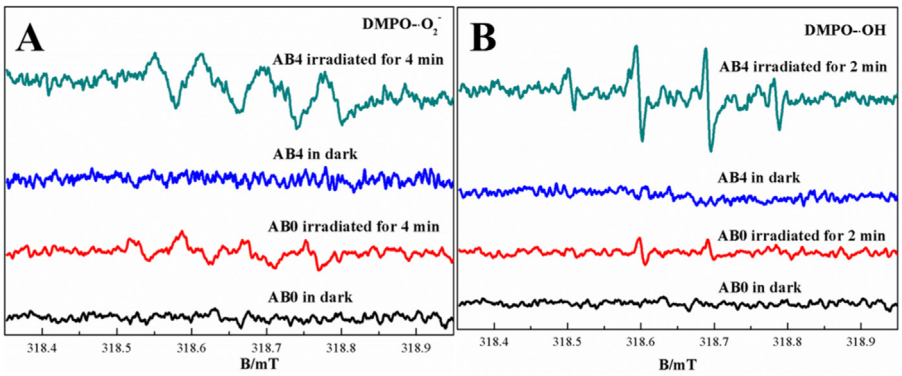

Fig. 9. DMPO spin-trapping ESR spectra by the samples AB0 and AB4 for detecting DMPO-·O_2^- (A) and DMPO-·OH (B) in deionized water and methanol, respectively.

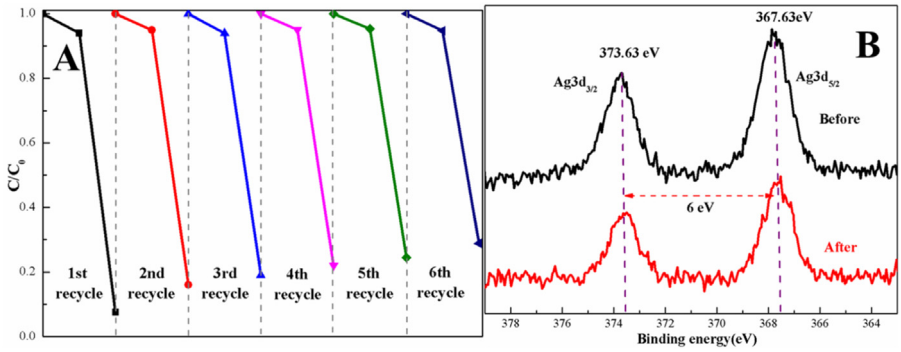

Fig. 10. Reusability tests of the composite AB4 for degradation of RhB under visible-light irradiation (A), and the Ag 3d XPS of the composite AB4 before and after reusability tests (B).

later ensures the efficient access of contaminant molecules to active sites and the subsequent escape of mineralized products or intermediates [37,38]. As a result, a synergistic effect of the strengthened light harvesting ability, efficient separation of charge carriers by LSPR effect, and the favorable electronic structure and morphology enables these Ag-containing bismuth-based composites to exhibit an excellent photocatalytic performance.

To explore the mechanism of the photocatalytic degradation, trapping experiments of active radical species were conducted over the sample AB4, as depicted in Fig. 8A. It is obvious that the photocatalytic performance becomes quite low after adding the reagent EDTA-2Na, holes trapper, indicating that holes were predominate active species during the photocatalytic process. Nevertheless, the addition of IPA, hydroxyl radical trappers, has almost no effect, revealing that the formation of radicals •OH is a minor factor determining the catalytic efficiency [39]. Generally, the existence of •O_2^- radicals can be detected by the abatement of NBT concentration during photocatalysis since NBT molecules are apt to react with produced •O_2^- radicals to yield insoluble intermediate purple formazan [24]. Consequently, an obvious decrease of NBT concentration was observed in experimental and hereby contributed to the presence of •O_2^- radicals in Fig. 8B. To further demonstrate the presence of both •OH and •O_2^- species, ESR technique was adopted by using DMPO as a scavenger and represented in Fig. 9. As can be observed, neither composite AB4 nor sample AB0 shows any signals in dark. Under visible irradiation for several minutes, both samples exhibit evident several signals corresponding to ·OH and •O_2^- radicals. The intensity of •O_2^- species signals of composite AB4 is much stronger than that of sample AB0 in Fig. 9A, revealing the more •O_2^- species generated by the composite AB4 than the sample AB0 [40]. The similar tendency can be found for the formation of ·OH radicals in Fig. 9B. In addition, the variation consistency of both •OH and •O_2^- species signals reveals the possible conversion of •O_2^- to •OH radicals under such a circumstance.

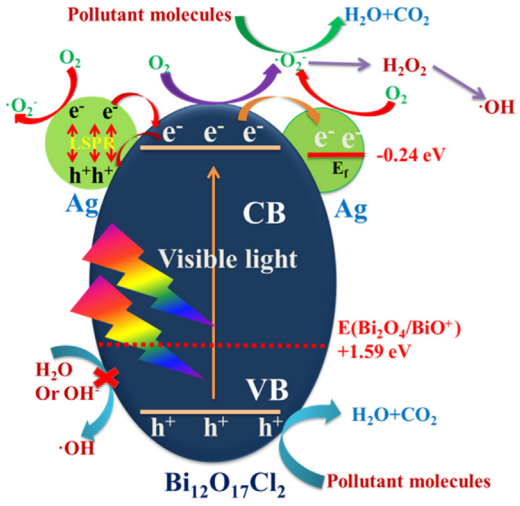

Scheme 1. The charge carriers separation and proposed photocatalysis mechanism of the composite AB4 upon visible-light irradiation.

On the basis of experimental results, a schematic band alignment between the metallic Ag nanoparticles and $Bi_{12}O_{17}Cl_2$ semiconductor was shown to propose a photocatalysis mechanism upon the degradation of organic contaminants in Scheme 1. According to the speculation in the XPS section, the work function of metallic Ag is smaller than that of semiconductor $Bi_{12}O_{17}Cl_2$ and thus the Fermi level of $Bi_{12}O_{17}Cl_2$ is lower than that of Ag, resulting in the efficient transfer of electrons from Ag to $Bi_{12}O_{17}Cl_2$ through the interface of metal-semiconductor, namely the ohmic contact,

till a new Fermi level is generated between two systems [41]. Under the visible-light irradiation, the semiconductor $Bi_{12}O_{17}Cl_2$ is excited and electrons can transfer from the valence band to the conduction band, leaving holes behind. Since the top of conduction band (-0.44 eV) of $Bi_{12}O_{17}Cl_2$ is much negative than the Fermi level of metallic Ag (-0.24 eV NHE) [42], the electrons on the $Bi_{12}O_{17}Cl_2$ conduction band are thermodynamically transferred across the interface of metal-semiconductor phase to Ag nanoparticles that are generally realized to role as sinks to accumulate photogenerated electrons, thus benefiting the separation of charge carriers and further the enhancement of photocatalytic efficiency. In addition, after harvesting the incident visible light with specific frequencies, Ag nanoparticles undergo an excitation that promotes electron around the Fermi energy level to move to the LSPR state and correspondingly holes leaved are able to combine with photogenerated electrons from the conduction band of $Bi_{12}O_{17}Cl_2$. Because of the high fluidity, the electrons on Ag nanoparticles easily reduce the surface-adsorbed oxygen molecules to $\cdot O_2^-$ species, thus effectively inhibiting the recombination of produced charge carriers. In addition, the electrons retained on the conduction band of $Bi_{12}O_{17}Cl_2$ can react with O_2 to produce $^\bullet O_2^-$ radicals as well since the E_{CB} of $Bi_{12}O_{17}Cl_2$ (-0.44 eV) is much negative than the redox potential $E(^\bullet O_2^-/O_2)$ (-0.046 eV) [43]. The standard redox potential of Bi_2O_4/BiO^+ (Bi^V/Bi^{III}) (+1.59 eV) in water solution is generally adopted to estimate the oxidation capability of holes in bismuth-based photocatalysts since holes in the valence band of Bi^{3+} are considered as Bi^{5+} or Bi^{4+} [44]. Significantly, the value is more negative than those of $E(\cdot OH/H_2O)$ (+2.68 eV) and $E(\cdot OH/OH^-)$ (+1.99 eV) and the formation of $^\bullet OH$ radicals is theoretically impossible by this manner [40,43]. Consequently, the $^\bullet OH$ radicals can only be produced by a chain reaction of single-electron reduction of O_2 to produce $^\bullet O_2^-$, then H_2O_2, and eventually $\cdot OH$ [45]. As a result, several kinds of species such as holes, $^\bullet O_2^-$ and $^\bullet OH$ can be generated in the photocatalytic process, during which both holes and $^\bullet O_2^-$ species are major reactive species to exert oxidative degradations under the visible-light illumination.

The reusability is another vital parameter for photocatalysts from a point of practical application of view. Hence, a successive recycling test was performed using the composite AB4, as shown in Fig. 10A. A slight decrease of photocatalytic efficiency is observed after six recycles, which may possibly attributed to the tiny photo corrosion of Ag species [46]. The release of Ag species could be realized by the slight decrease of Ag 3d signals intensity in Fig. 10B. Besides, there is no significant change for characteristic signals in XRD patterns before and after reaction in Fig. S4. As analyzed, the phase transformation and valence fluctuation of the composite AB4 did not occur. As a result, the as-synthesized Ag-containing plasmonic composite has an excellent stability and regeneration ability and can be potentially utilized in environmental protection and remediation fields.

4. Conclusion

A series of Ag-containing $Bi_{12}O_{17}Cl_2$ plasmonic composites were prepared via a simple two-step procedure and systematically characterized by various spectroscopic analyses. It was confirmed that metallic Ag nanoparticles were successfully deposited and uniformly dispersed on the surface of $Bi_{12}O_{17}Cl_2$. In addition, the Ag content in composites played an important role on optical and textural properties, and further on the photocatalytic capabilities. The composite AB4 with an optimized Ag mass percentage of 4% exhibited the best photocatalytic activity and the corresponding apparent reaction rate constants for degradation of RhB and 2,4-DCP were 5.3 and 1.7 times as high as those of pure $Bi_{12}O_{17}Cl_2$, respectively. The significant enhancement of $Ag/Bi_{12}O_{17}Cl_2$ photocatalytic performance might be ascribed to a synergistic effect of the efficient charge separation caused by the LSPR effect of metallic Ag nanoparticles, strong visible-light harvesting and favorable morphology with enlarged specific surface areas. Finally, the photocatalytic mechanism over the $Ag/Bi_{12}O_{17}Cl_2$ composites was speculated according to the reactive radicals trapping experiments.

Acknowledgements

We are grateful to the National Natural Science Foundation of China (No. 21207089), the project-sponsored by SRF for ROCS, SEM., the Hujiang Foundation of China (No. B14003), the Innovation Program of Shanghai Municipal Education Commission (No. 14ZZ136), and the Natural Science Foundation of Shanghai (No. 13ZR1427600) for financial support.

Appendix A. Supplementary data

Supplementary data associated with this article can be found, in the online version, at http://dx.doi.org/10.1016/j.molcata.2016.11.028.

References

[1] X. Chen, S.S. Mao, Chem. Rev. 107 (2007) 2891–2959.
[2] A. Kubacka, M. Fernandez-Garcia, G. Colon, Chem. Rev. 112 (2012) 1555–1614.
[3] H.L. Wang, L.S. Zhang, Z.G. Chen, J.Q. Hu, S.J. Li, Z.H. Wang, J.S. Liu, X.C. Wang, Chem. Soc. Rev. 43 (2014) 5234–5244.
[4] H.F. Cheng, B.B. Huang, Y. Dai, Nanoscale 6 (2014) 2009–2026.
[5] J. Li, Y. Yu, L.Z. Zhang, Nanoscale 6 (2014) 8473–8488.
[6] Y.C. Xie, F. Chang, C.L. Li, J. Chen, J.R. Luo, L. Li, X.F. Hu, Clean-Soil Air Water 42 (2014) 521–527.
[7] X. Xiao, C. Liu, R.P. Hu, X.X. Zuo, J.M. Nan, L.S. Li, L.S. Wang, J. Mater. Chem. 22 (2012) 22840–22843.
[8] X.Y. Xiao, J. Jiang, L.Z. Zhang, Appl. Catal. B 142 (2013) 487–493.
[9] X.Y. Chen, H.S. Huh, S.W. Lee, J. Solid State Chem. 180 (2007) 2510–2516.
[10] F. Chang, J.R. Luo, X.F. Wang, Y.C. Xie, B.Q. Deng, X.F. Hu, J. Colloid Int. Sci. 459 (2015) 136–145.
[11] G.P. He, C.L. Xing, X. Xiao, R.P. Hu, X.X. Zuo, J.M. Nan, Appl. Catal. B 170 (2015) 1–9.
[12] L.C. Tien, Y.L. Lin, S.Y. Chen, Mater. Lett. 113 (2013) 30–33.
[13] C.J. Bi, J. Cao, H.L. Lin, Y.J. Wang, S.F. Chen, Materi. Lett. 166 (2016) 267–270.
[14] J. Li, G.M. Zhan, Y. Yu, L.Z. Zhang, Nature Commun. 7 (2016).
[15] S.M. Lam, J.C. Sin, A.R. Mohamed, Mater. Sci. Semicond. Process. 47 (2016) 62–84.
[16] P. Zhang, T. Wang, X.X. Chang, J.L. Gong, Acc. Chem. Res. 49 (2016) 911–921.
[17] P. Zhang, T. Wang, J.L. Gong, Adv. Mater. 27 (2015) 5328–5342.
[18] J. Di, J.X. Xia, M.X. Ji, B. Wang, S. Yin, Y. Huang, Z.G. Chen, H.M. Li, Appl. Catal. B 188 (2016) 376–387.
[19] H. Liu, W.R. Cao, Y. Su, Y. Wang, X.H. Wang, Appl. Catal. B 111 (2012) 271–279.
[20] X.C. Zhang, B.Q. Lu, R. Li, X.L. Li, X.Y. Gao, C.M. Fan, Sep. Purif. Technol. 154 (2015) 68–75.
[21] T.T. Li, L.H. Zhao, Y.M. He, J. Cai, M.F. Luo, J.J. Lin, Appl. Catal. B 129 (2013) 255–263.
[22] X.F. Hu, T. Mohamood, W.H. Ma, C.C. Chen, J.C. Zhao, J. Phys. Chem. B 110 (2006) 26012–26018.
[23] F. Chang, J. Zhang, Y.C. Xie, J. Chen, C.L. Li, J. Wang, J.R. Luo, B.Q. Deng, X.F. Hu, Appl. Sur. Sci. 311 (2014) 574–581.
[24] L.Q. Ye, J.Y. Liu, Z. Jiang, T.Y. Peng, L. Zan, Appl. Catal. B 142 (2013) 1–7.
[25] M. Niederberger, H. Colfen, Phys. Chem. Chem. Phys. 8 (2006) 3271–3287.
[26] W.W. Lu, G.S. Liu, S.Y. Gao, S.T. Xing, J.J. Wang, Nanotechnology 19 (2008).
[27] M. Faisal, A.A. Ismail, F.A. Harraz, S.A. Al-Sayari, A.M. El-Toni, M.S. Al-Assiri, Mater. Des. 98 (2016) 223–230.
[28] D.B. Xu, W.D. Shi, C.J. Song, M. Chen, S.B. Yang, W.Q. Fan, B.Y. Chen, Appl. Catal. B 191 (2016) 228–234.
[29] A. Sarkar, S. Kapoor, T. Mukherjee, Res. Chem. Intermed. 36 (2010) 411–421.
[30] J. Xu, L.W. Zhang, R. Shi, Y.F. Zhu, J. Mater. Chem. A 1 (2013) 14766–14772.
[31] S. Bai, X.Y. Li, Q. Kong, R. Long, C.M. Wang, J. Jiang, Y.J. Xiong, Adv. Mater. 27 (2015) 3444–3452.
[32] S.L. Ma, S.H. Zhan, Y.N. Jia, Q. Shi, Q.X. Zhou, Appl. Catal. B 186 (2016) 77–87.
[33] N.A. Ramos-Delgado, M.A. Gracia-Pinilla, L. Maya-Trevino, L. Hinojosa-Reyes, J.L. Guzman-Mar, A. Hernandez-Ramirez, J. Hazard. Mater. 263 (2013) 36–44.
[34] L. Ge, C.C. Han, J. Liu, Y.F. Li, Appl. Catal. A 409 (2011) 215–222.
[35] X. Xin, J.Y. Lang, T.T. Wang, Y.G. Su, Y.X. Zhao, X.J. Wang, Appl. Catal. B 181 (2016) 197–209.
[36] X.X. Hu, C. Hu, R. Wang, Appl. Catal. B 176 (2015) 637–645.
[37] J.G. Yu, Y.R. Su, B. Cheng, Adv. Funct. Mater 17 (2007) 1984–1990.
[38] J.G. Yu, L.J. Zhang, B. Cheng, Y.R. Su, J. Phys. Chem. C 111 (2007) 10582–10589.

[39] Y.Y. Zhu, Y.F. Liu, Y.H. Lv, Q. Ling, D. Liu, Y.F. Zhu, J. Mater. Chem. A 2 (2014) 13041–13048.
[40] F. Dong, Z.W. Zhao, Y.J. Sun, Y.X. Zhang, S. Yan, Z.B. Wu, Environ. Sci. Technol. 49 (2015) 12432–12440.
[41] A. Wood, M. Giersig, P. Mulvaney, J. Phys. Chem. B 105 (2001) 8810–8815.
[42] M. Lei, W. Wu, L.L. Sun, Q.Y. Tian, C.Z. Jiang, X.H. Xiao, Colloids Surf. A 482 (2015) 276–282.
[43] H.F. Li, H.T. Yu, X. Quan, S. Chen, Y.B. Zhang, Acs Appl. Mater. Int. 8 (2016) 2111–2119.
[44] F.T. Li, Q. Wang, X.J. Wang, B. Li, Y.J. Hao, R.H. Liu, D.S. Zhao, Appl. Catal. B 150 (2014) 574–584.
[45] Q.J. Xiang, J.G. Yu, B. Cheng, H.C. Ong, Chem. Asian J. 5 (2010) 1466–1474.
[46] H.J. Dong, G. Chen, J.X. Sun, Y.J. Feng, C.M. Li, C.D. Lv, Chem. Commun. 50 (2014) 6596–6599.